Experimental investigation of the effect of blade solidity on micro-scale and low tip-speed ratio wind turbines

Martin Bourhis, Michaël Pereira, Florent Ravelet

Experimental investigation of the effect of blade solidity on micro-scale and low tip-speed ratio wind turbines

M. Bourhis[a,*], M. Pereira[a], F. Ravelet[a]

[a] *Arts et Metiers Institute of Technology, CNAM, LIFSE, HESAM University, 75013 Paris, France*

Abstract

It is well-established that micro-scale wind turbines require high blade solidity in order to overtake friction torque of all mechanical parts and starts operating. Therefore, multi-bladed micro-scale rotors with a low design tip-speed ratio λ are advocated. However, no consensual blade solidity is admitted by the scientific community at low Reynolds number and low tip-speed ratio because the reliability of the airfoil data, used in the blade element momentum theory, is questionable. The vast majority of the open literature has focused on the number of blades rather than varying blade chord length to increase the solidity. This experimental study carried out in a wind tunnel serves two purposes: to examine blade solidity effect on the power C_p and torque coefficients C_τ vs. tip-speed ratio curves at a fixed number of blades and to investigate its effects on the velocity distributions using stereoscopic particle image velocimetry (SPIV) for three tip-speed ratio $\lambda = 0.5$, $\lambda = 1$ and $\lambda = 1.4$. Six 200 mm diameter runners with 8 blades and various blade solidity from $\sigma = 1.5$ to $\sigma = 0.5$ were designed at $\lambda = 1$ without using airfoil data. The results emphasize that the maximum power coefficient increases with blade solidity up to a maximum value $C_{p,max} = 0.29$ reached for $\sigma = 1.25$. High-solidity rotors have a very low cut-in wind speed $V_0 = 3.8$ m.s^{-1} and their torque coefficient C_τ decreases drastically and linearly while increasing the tip-speed ratio λ. These specificities could be of particular interest for energy harvesting of low speed air flow in order to power low-energy appliances. However, for low-solidity rotors, the C_τ vs. λ curves present a similar trend than the lift coefficient vs. angle of attack polar plots of isolated airfoil which is characterised by a significant drop in C_τ illustrating stall effect. An increase in blade solidity postpones and attenuates the stall effects due to greater mutual blade interactions. The SPIV recordings reveal that for high-solidity rotors the magnitude and radial profiles of axial and tangential induction factors and the flow deflection were close to the design settings. Moreover, the analysis exhibits that an increase in the blade solidity and tip-speed ratio leads to higher axial and tangential induction factors. The investigation of the wake highlights that the aerodynamic torque generated by a wind turbine is not produced in a same way as changing the blade solidity or the tip-speed ratio. To conclude, the best compromise between the maximum power coefficient, the cut-in wind speed, the mass of filament and the stability of the wake is achieved for the rotor with a blade solidity of $\sigma = 1.25$.

Keywords: Wind energy harvesting, micro-scale wind turbine, blade solidity, power and torque coefficients, stereoscopic particle image velocimetry

1. Introduction

Wind energy plays a crucial role in the reduction of the greenhouse gases emissions. With the help of scientific research, the performance, size and design of wind machines have greatly evolved from multi-bladed windmills prior to 19^{th} century used for pumping water and milling grain to three-bladed horizontal axis wind turbines (HAWT) widely used for electricity generation in the developed countries. This fast and dynamic development has been followed by a 27% increase of the installed wind power capacity in Europe from 2018 to 2019 [1]. The most efficient rotors at large-scale, *i.e.* rotors with diameter higher than 5.0 m, are three-bladed horizontal axis wind turbines operating at high tip-speed ratio λ defined as follows:

$$\lambda = \frac{R_T \omega}{V_\infty} \quad (1)$$

where $R_T\omega$ is the tip-velocity and V_∞ is the freestream wind velocity. They can convert up to $40 - 50\%$ of the kinetic power of the wind into mechanical power at tip-speed ratio of the order of 6 to 7 [2–4].

Even though, large-scale wind turbines nowadays play a key role in the electricity production, there is also a growing interest in micro-scale wind turbines with the recent advances in energy harvesting [5]. These wind machines, with rotor diameter under 0.20 m, could harvest the energy of natural air circulation in building or outside to power low-energy appliances, especially in the field of the IOT [6–10]. Although there are many studies on large-scale run-

*corresponding author
Email address: martin.bourhis@ensam.eu (M. Bourhis)

ners, the research on micro-scale wind turbines remains limited. Some studies have focused on wind tunnel experiments with scaled-down wind turbines in order to get scaling laws and laws of similarity rather than designing efficient micro-scale runners. Consequently, the vast majority of prototypes found in the open literature achieves lower performance than large-scale runners [11, 12].

The high efficiency of the conversion of kinetic to mechanical power by large-scale wind turbines is achieved thanks to the aerodynamic optimisation of the blades through the choice of the chord c and pitch angle distributions ϕ (Fig. 1), the number of blades, the operating optimum tip-speed ratio and the airfoil shape. Their design is based on two independent theories: the general momentum theory and the blade element method. This method is widely used by wind turbine manufacturers for the design or the analysis of existing rotors and is commonly known as the Blade Element/Momentum Theory (BEMT).

The design of micro-scale wind turbines differs from the design of larger ones to achieve the highest efficiency in low wind speed conditions. A high torque is required at low wind speed to start running and producing power. To meet this requirement, their design tip-speed ratio is significantly lower than the design tip-speed ratio of large-scale turbines. A high solidity σ and number of blades N are also recommended to increase the torque and thus reducing the cut-in wind speed [13–17]. It explains why most of the micro-scale wind turbines found in the open literature are multi-bladed and have a large solidity [6, 18–20]. The local blade solidity is defined as the ratio of blade chord length to spacing:

$$\sigma = \frac{Nc}{2\pi r} \tag{2}$$

where r is the spanwise coordinate.

The blade solidity has a significant influence in the starting behaviour and in the efficiency of a micro-scale runner. Indeed, from a practical standpoint, an infinite blade solidity would not allow the fluid to pass through the rotor plane. On the contrary, a solidity equal to $\sigma = 0$ implies that the wind turbine is transparent to the fluid. In both cases, no power conversion is achieved [15]. Considering a high-solidity rotor, the fluid would strictly follow the deflection imposed by the blade geometry. The flow relative angle in the near wake of the rotors would at least be equal to the blade trailing edge angle. By reducing the blade solidity, the difference between the blade angle and the outlet flow angle becomes more significant.

Although there exist a considerable body of literature about the relationship between the number of blades and the performance of a rotor, the effect of blade solidity on wind turbine performances, starting behaviour and wake characteristics is still an open question. As far as we know, only a few works has experimentally investigated the effect of the blade solidity on the flow velocity distribution in the near wake of a wind turbine. It could be of particular interest to perform this experimental investigation in order to provide a better understanding of the mechanism of flow deflection. This study would provide the scientific literature with a set of data illustrating the mechanism of torque creation by a wind turbine.

The absence of consensual optimal blade solidity for micro-scale runners is partly explained by the limitations of the classical design method, the BEMT, to compute the blade solidity of micro-scale rotors with a low design tip-speed ratio. The definitions and results of the general momentum theory relevant to this study are documented in Appendix A. Even though the general momentum and the blade element theories are efficient to design low-solidity large-scale runners operating at high tip-speed ratio, three major issues arise when the diameter and tip-speed ratio decrease.

First, optimal flow conditions based on the Glauert's model are widely recognised by the scientific community at high tip-speed ratio ($\lambda \geq 3$), however there is no agreement at lower tip-speed ratios. For instance, large differences in the axial a and tangential a' induction factors, defined in Eqs. A.2 & A.3, are observed between the models of Sørensen [21], Joukowksi [5]joukowsky1912, Burton [22], Glauert [23] and Betz [24] at $\lambda = 1$ (§ 4 in Ref.[21]). At low tip-speed ratio, the blade solidity distribution differs significantly between these models. The relevance of one model or the other for the design is briefly adressed in the literature and the choice of a and a' remains arbitrary.

Secondly, the blade element theory, used to design low-solidity and large-scale wind turbines, suffers from some limitations for the design of high-solidity micro-scale runners. This method relies on the airfoil lift and drag polar diagrams to compute the blade solidity and pitch angle. The aim of the method is to compute the local force on many independent blade elements with the aerodynamic coefficients and optimal induction factors in order to match with the lift force computed from the general momentum theory. Therefore, the optimal blade solidity and pitch angle are highly dependent on the accuracy of the airfoil data. Due to their small size, micro-scale wind turbines operate at low Reynolds number ($Re \leq 10^5$) where the laminar-turbulent transition occurs. Very few experimental data on aerodynamic airfoil are available in this range of Reynolds number. Consequently, micro-scale wind turbines are designed with high Reynolds number airfoil data. The validity of the optimum angle of attack and aerodynamic coefficients is questionable and the relevance of the blade element theory to compute an optimal blade solidity for micro-scale runners is doubtful.

Thirdly, at low tip-speed ratio, the blade solidity computed with the Glauert's optimal distributions of a' and a is high (§ 4 in Ref.[21]). It raises the question of the mutual interaction between blades which shed further doubts on the airfoil data. Sharpe in Ref [25] highlights the difficulty to design high-solidity wind turbine: "[...]the only available blade element data are for isolated, two dimensional airfoils. The mutual interactions between the closely spaced, probably overlapping, blades would be large and so

the available airfoil data would be useless for the purpose of designing high-solidity wind turbines".

Bourhis et al. in Ref [11] proposed an alternative method to design high-solidity wind turbines without using the airfoil data. The goal of the method is to design a high-solidity blade cascade arrangement which is able to deflect the airflow as desired. In this work, the blade angles of a 300 mm turbine were calculated by assuming a constant axial induction factor and a constant tangential velocity in the wake. The blade solidity was arbitrary set from $\sigma = 1.65$ at the root to $\sigma = 0.7$ at the tip. The authors assumed that this solidity will ensure the required flow deflection. The performance and wake characteristics of the rotors were collected from wind tunnel experiments. It presented a high maximum power coefficient $C_{p,max} = 0.31$ (Eq. A.5) at low tip-speed ratio $\lambda = 1$, a linear evolution of its torque coefficient C_τ (Eq. A.6) with the tip-speed ratio λ and a highly stable and rotating wake. However, discrepancies were observed between the outlet blade geometric angle and the relative flow angle in the wake. It suggests that the solidity was not high enough to ensure the required flow deflection. Finally, the authors address the need for improvement of the design method and they suggest, in particular, further investigations on the blade solidity effect on the flow deflection, performance and starting behaviour of a micro-scale runner. This research topic is barely addressed in the literature although it is of great interest for the design of efficient micro-scale turbines.

The study of the blade solidity effect on the rotor performance and wake can be carried out by changing either the number of blades N or the chord length c (Eq. 2). Previous studies have primarily focused on the blade number effect on wind turbine power coefficient C_p and torque coefficient C_τ. Some of them suggests that increasing the number of blades while keeping a same blade gemetry leads to increase the maximum power coefficient $C_{p,max}$, especially when the rotor operates at low wind speed and tip-speed ratio [20, 26, 27] or at low Reynolds number [28]. However, some authors draw contradictory conclusions [15–17]. Rector and Visser added in Ref. [29] that the maximum power coefficient increases with the blade solidity at low wind speed but not at high wind speed.

Leung et al. in Ref.[20] performed a CFD investigation of the effect of the blade solidity and they concluded that a solidity higher than 0.5 is favored for the design of efficient micro-scale wind turbines.

Brasil et al. in Ref. [30] carried out wind tunnel experiments with 200 mm rotors with $N = 2$, 3 and 4 blades. The rotors were designed at $\lambda = 1.6$ according to the BEMT with the Glauert's optimal flow conditions and tip-loss factor. By adding the tip-loss factor, the blade solidity differs from a configuration to another even though the design tip-speed ratio remains the same. They reported that increasing the number of blades while keeping a same design tip-speed ratio leads to higher torque coefficient, especially at low tip-speed ratio, and higher maximum power coefficient. Higher torque coefficient at low λ induces lower cut-in wind speed that is require to harvest the energy of low-speed airflow.

Duquette et al. discuss the effect of the number of blades and solidity on the performance of a 1 m diameter rotor [15]. Firstly, a rotor with flat plate blades (constant chord and non-twisted blades) was experimentally studied in 5 configurations (N,σ) : $(3, 0.07)$, $(3, 0.14)$, $(3, 0.27)$, $(6, 0.14)$ and $(12, 0.27)$. The results suggest that an increase in the number of blades at fixed solidity leads to very small changess in power coefficient curves and in the maximum power coefficient. However, as blade solidity was increased at fixed number of blades, the power coefficient increased. A second rotor with a set of blades designed according to the BEMT was tested in five configurations $(3, 0.05)$, $(3, 0.1)$, $(3, 0.15)$, $(6, 0.1)$, $(12, 0.1)$. The results pointed out the increase in the maximum power coefficient with the blade solidity at fixed number of blades and the decrease in the power coefficient with the number of blades at fixed blade solidity. Although, this experimental study provides relevant results, the geometry of the blades were not modified between acquisitions as it should be according to the Glauert's optimal distribution of a and a'.

A recent study by Eltayesh et al. highlights that adding identical blades decreases the maximum power coefficient and tip-speed ratio but increases the torque coefficient and therefore reduces the cut-in wind speed [16]. However, the blade solidity and range of study is low and consequently the operating tip-speed ratio range of the rotor is too high for low wind speed applications. Similar conclusions are reported by Wang and Chen in Ref. [17]. They also argue that the decrease in the power coefficient could be the result of a strong fluid blockage by high-solidity turbines.

Duquette and Visser in Ref. [31] numerically investigate blade number and solidity effect on the performance of a 2 m diameter rotor with the BEMT and the lifting line wake theory. The number of blades varies from $N = 3$ to $N = 12$ and the blade solidity from $\sigma = 0.05$ to $\sigma = 0.43$. Their study shows that an increase in blade number increases the maximum power coefficient at a given solidity. Moreover, they found that an increase in the solidity from $\sigma = 0.05$ to $\sigma = 0.25$ leads to higher maximum power coefficient and lower optimum tip-speed ratio. In addition, they found an optimum solidity that maximises the power coefficient for a fixed number of blades.

Another recent experimental study by Zawadzki et al. in Ref. [27] reports other conclusions. They performed wind tunnel experiments with a 400 mm wind turbine equipped with blades with constant chord length. They varied independently the number of blades ($N = 2, 3, 4$) and the chord length ($c = 0.02$ m, 0.0266 m). The results suggest that an increase in the blade chord length *i.e.* in the blade solidity at fixed number of blades increases the power coefficient and decreases the optimum tip-speed ratio. One can regret that the range of blade solidity is very limited but the authors bring some inter-

esting information. Moreover, unlike Eltayesh et al. the authors reported an increase in the power coefficient with the number of blades at fixed blade geometry. Finally, the authors concluded that at a fixed solidity, an increase in the chord length has more valuable effect on the power coefficient than an increase in the number of blades.

Overall these studies highlight a strong effect of the blade solidity on the performance and starting behaviour of micro-scale runners. Most experimental investigations have examined the blade number effect on the power and torque coefficients of low-solidity rotor ($\sigma \leq 1$) designed to operate at high tip-speed ratio ($\lambda \geq 3$). The literature on the effect of the blade solidity at fixed number of blades is less consistent. Moreover, the effect of the blade solidity on the flow velocity distributions in the near wake of a turbine is barely adressed. To our knowledge, no prior studies have performed a full experimental investigation of the effect of the blade solidity at fixed number of blades on micro-scale runner's performance and wake.

Therefore, to fill this literature gap, the aim of this experimental study is to investigate the effect of the blade solidity on performance and wake of six 200 mm diameter wind turbines. The design of the rotors with various solidity is detailed in § 2. The experimental apparatus to obtain the performance for various operating points is presented in § 3. It contains also a description of the stereoscopic particle image velocimetry (SPIV) setup implemented to investigate the flow velocity distributions in the near wake of each runner. The experimental results are presented and analysed in § 4. Finally, overall conclusions and perspectives of this work are discussed in § 5.

2. Design method

Six micro-scale wind turbines were designed according to the method of Bourhis et al. presented in Ref. [11] with a different vortex law. With the exception of the blade solidity σ, all runners are designed with the same parameters. Their design tip-speed ratio is equal to $\lambda = 1$ and they have $N = 8$ blades. Tip and hub radius are respectively $R_T = 100$ mm and $R_H = 30$ mm, therefore, the hub ratio is $H = 0.3$.

As mentioned in the § 1, the purpose of the method is to design a high-solidity blade cascade wind turbine which is able to drive and deflect the air flow as desired. The procedures used to compute the blade angles and the chord length distributions are described in the § 2.1 and in the § 2.2. The manufacturing process is detailed in the § 2.3.

2.1. Blade angles

The blade angles at the inlet β_1 and outlet β_2 of the cascade are defined according to the velocity triangle (please see Fig.1). β is the angle between the rotor plane and the relative velocity. Index 1 and 2 refer respectively to the inlet and outlet of the cascade. The spanwise variations of β_1 and β_2 are computed for 11 sections from the root to the tip of the blade and read:

$$\beta_1 = arctan\left(\frac{C_1}{U}\right) \quad (3)$$

$$\beta_2 = arctan\left(\frac{C_{z2}}{U + C_{\theta 2}}\right) \quad (4)$$

where C is the absolute velocity, U is the rotating velocity of the rotor and C_z and C_θ are the axial and tangential absolute velocities. The velocity distributions are computed according to the general momentum theory introduced in

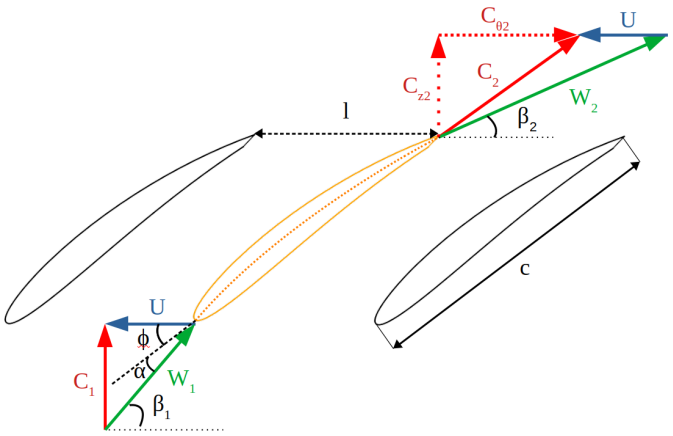

Figure 1: From Bourhis et. al [11]. Velocity triangles at the input (index 1) and output (index 2) of the blade cascade arrangement. U, C and W are respectively the body rotating, absolute and relative velocities. C_θ and C_z are the tangential and axial fluid velocities. The blade solidity σ is the ratio of the blade chord length c to spacing l *i.e.* $\sigma = c/l$. ϕ is the pitch angle and α the angle of attack

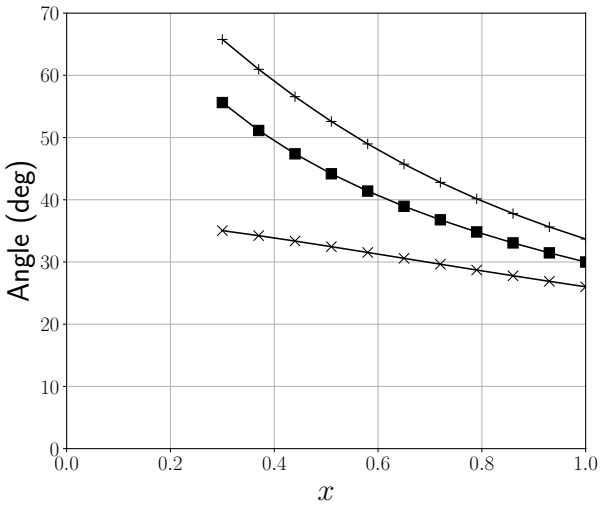

Figure 2: Spanwise variations of inlet β_1 (+) and outlet β_2 (×) relative angles. The pitch angle distribution (■) is computed according to the Eq. 10

the Appendix A and read:

$$C_1 = C_{z1} = C_{z2} = V_\infty(1-a) \quad (5)$$
$$C_{\theta 2} = 2a'\omega r \quad (6)$$

Therefore, the Eqs. 3 & 4 read:

$$\beta_1 = arctan\left(\frac{R_T(1-a)}{\lambda x}\right) \quad (7)$$
$$\beta_2 = arctan\left(\frac{R_T(1-a)}{\lambda x(1+2a')}\right) \quad (8)$$

The blade angles only depend on the local tip-speed ratio and on the induction factors, consequently the distributions are the same for all six rotors. For the design of the rotors, the axial induction factor is set at $a = 1/3$ and the tangential induction factor is computed according to the Glauert's optimum distribution for $\lambda = 1$ (Eqs. A.9 & A.10). The spanwise variations of the blade cascade relative angles for all six runners are shown in Fig.2.

Then, a polynomial camber mean-line, tangent to the relative velocity at the leading and trailing edge, is drawn for the 11 radius:

$$Y = \frac{tan(\beta_2) - tan(\beta_1)}{2}X^2 + tan(\beta_1)X \quad (9)$$

with $X \in [0;1]$. The camber mean-line is upscaled with the blade solidity distribution (discussed in the next subsection § 2.2) and thickened according to the thickness distribution of the symmetric NACAxx10 airfoil. The pitch angle *i.e.* the angle between the rotor plane and the chord line reads:

$$\phi = arctan\left(\frac{tan(\beta_1) + tan(\beta_2)}{2}\right) \quad (10)$$

The angle between the rotor plane and the relative velocity varies at the inlet from $\beta_1 = 66°$ to $\beta_1 = 34°$ and from $\beta_2 = 35°$ to $\beta_2 = 26°$ at the outlet. Consequently, the theoretical airflow deflection $|\Delta\beta| = |\beta_2 - \beta_1|$ in the rotor's reference frame decreases from $|\Delta\beta| = 31°$ at the root of the blade to $|\Delta\beta| = 8°$ at the tip. No empirical coefficients or loss models are applied in the design method to correct the blade angles. The blades are twisted from $\phi = 56°$ a the hub to $\phi = 30°$ at the tip. In comparison, the pitch angle decreases from $\phi = 43°$ to $\phi = 25°$ when the turbine is designed according to the classical BEMT method with a SG6042 airfoil and a fixed angle of attack $\alpha = 6°$, where α is the angle between the inlet relative velocity and chord length (Fig.1). The blade pitch angle is significantly higher with the actual design method and the blades are more twisted.

With the present design tip-speed ratio $\lambda = 1$ and induction factors, the theoretical maximum power coefficient is $C_{p,max} = 0.383$ (Eq. A.7). The theoretical torque coefficient at the design tip-speed ratio is also equal to $C_\tau(\lambda = 1) = 0.383$ (Eq. A.8).

2.2. Blade solidity

One objective of this study is to investigate the effect of the blade solidity σ on the flow deflection *i.e.* on the difference between the design blade outlet relative angle and the relative flow angle in the near wake of the turbines.

In the theoretical case of an inviscid and laminar flow, a high solidity turbine would perfectly constrain the flow into the cascade arrangement and the deflection and performance would be closed to the design values. Micro-scale wind turbines operate in open-flow and low Reynolds number conditions ($Re \leq 10^5$). An increase in friction losses from viscous interactions between the blades and the flow can lead to a drop in the deflection efficiency and a decrease in rotor performance. An excessive blade solidity could also prevent airflow from passing through the space between blades.

The literature review on micro-scale wind turbines has shown that these machines have a high blade solidity. Based on the available data and pictures, the blade solidity of micro-wind turbines found in the open literature were calculated. The runners of Zakaria et al. [18] and Howey et al. [19] have a blade solidity at the mid span approximately equal to $\sigma \approx 0.7$. Mendonca et al. studied micro-scale wind turbines with blade solidity from $\sigma = 0.25$ to $\sigma = 0.95$ [28].

In order to cover a wide range of solidity, 5 rotors with a constant solidity from $\sigma = 1.5$ to $\sigma = 0.5$ with steps of $\sigma = 0.25$ were designed. Another rotor with a variable solidity from $\sigma = 1.65$ at the root to $\sigma = 0.7$ at the tip was also designed. Its solidity was selected in order to have a quasi-constant chord length. For the other runners, a constant blade solidity along the span implies a linear variation of the chord length c according to the Eq. 2. Tip, middle and hub chord lengths are presented for each rotor in the first part of the Tab. 1. As shown in the second part of the Tab.1 the rotors operate in a wide range of Reynolds number. Low-solidity runners operate in lower Reynolds number than large-solidity rotors and therefore, the flow pattern in the blade cascade arrangement can vary strongly from high to low-solidity rotor. The axial length of the hub (42.5 mm) and the fillet radius (5 mm) are equal for all rotors. The third part of the Tab.1 shows the volume and the length of the runners. The length is defined as the maximum distance between the fillet of the hub and the trailing edge and the volume is the total volume of the blades and hub. Both rotor length and volume increase with the solidity. The use of one rotor or the other can be potentially justified by the space available in the implementation area, the printing time or the mass of filament if the providing performance remains the same (Tab.1).

The 3D CAD are presented in the Fig.3. The figure shows that the blade of high-solidity runners are thicker because of larger chord length. However, the relative thickness remains the same for all rotors. The figure clearly shows the increase in blade overlap with the solidity.

σ		1.5	1.25	1.00	0.75	0.50	$1.65-0.7$
$c(R_H)$	[mm]	35	29	24	18	12	39
$c(R_{mid})$	[mm]	77	64	51	38	26	47
$c(R_T)$	[mm]	118	98	79	59	39	55
$Re(R_H)$		25800	21500	17200	12900	8600	28400
$Re(R_T)$		141600	118000	94400	70800	47200	66100
Volume	[cm^{-3}]	356	281	213	162	128	186
Length	[mm]	66	56	46	36	27	34
Printing time	[h]	34	27	25	15	12	21
Filament mass	[g]	293	237	205	139	124	184

Table 1: Wind turbines design parameters. The chord length c is computed at the hub, midspan and tip of the blade. Reynolds number is computed according to $Re = \rho W_1 c/\eta$ where W_1 is the inlet relative velocity of the flow, ρ is the air density and η is the air dynamic viscosity. The length of the rotor is the maximal horizontal distance between the face of the hub and the trailing edge and the volume is the total volume of the blades and hub. Printing time and filament mass are obtained from fused material deposition (FMD) software

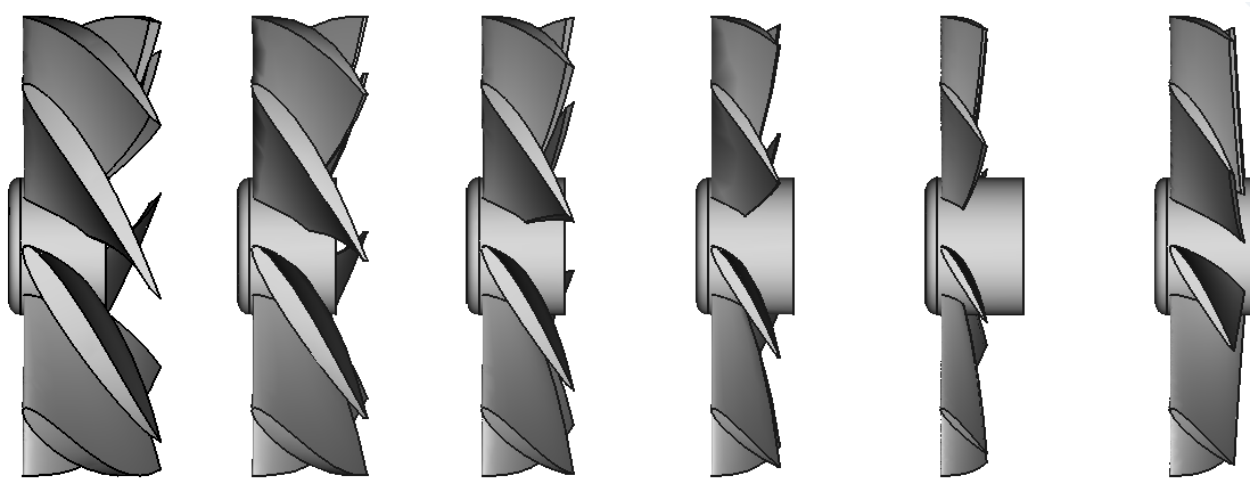

Figure 3: Side view of the 3D CAD of the six runners classified from $\sigma = 1.5$ to $\sigma = 0.5$. The last turbine on the right side has a variable solidity from $\sigma = 1.65$ at the hub to $\sigma = 0.7$ at the tip

2.3. Manufacturing process

The runners were manufactured by fused material deposition (FMD) with a commercial 3D printer CREALITY CR10SPRO. There is a growing interest to build micro-scale wind turbine prototype by FMD with the recent progress in this technology and the advent of affordable 3D printer. This manufacturing technology has already been used successfully to build small rotors prototypes [19, 30, 32]. The low cost of the 3D printer and filament materials, the high repeatability and speed of this process are relevant benefits to manufacture small rotors [33].

Polyactic acid (PLA) filament was used as print material for its low cost, high availability and basic printer requirements (low melting point, no need of heated bed). Moreover, PLA is also one of the most environmentally friendly materials available on the market.

The following printing parameters were selected in order to have a good balance between printing time and quality. The rotors were filled with a grid pattern of variable dimensions. The total infill percentage is equal to 20% which ensures good blade stiffness and processability without a dramatic increase in the printing time. The 3D printing support were generated automatically with a overhang threshold set at 45°. The layer height and printing speed were respectively set at 0.16 mm and 100 $mm.s^{-1}$.

Two rotors with same geometry were built to assess the repeatability of the manufacturing process. The curves $C_p - \lambda$ and $C_\tau - \lambda$ were experimentally determined for both rotors. A deviation under 2% in the power and torque coefficients were found for all tip-speed ratios.

The last part of the Tab.1 presents the printing time and the filament mass required to manufacture each wind turbine. As mentioned in the previous section, the high increase in the printing time and amount of filament to build high-solidity rotors can justified the choice of low-solidity rotor if the performance are equal.

3. Experimental apparatus

The purpose of the experimental investigation is twofold: firstly, to obtain the power and torque coefficient for a wide range of tip-speed ratio; and secondly to investigate the

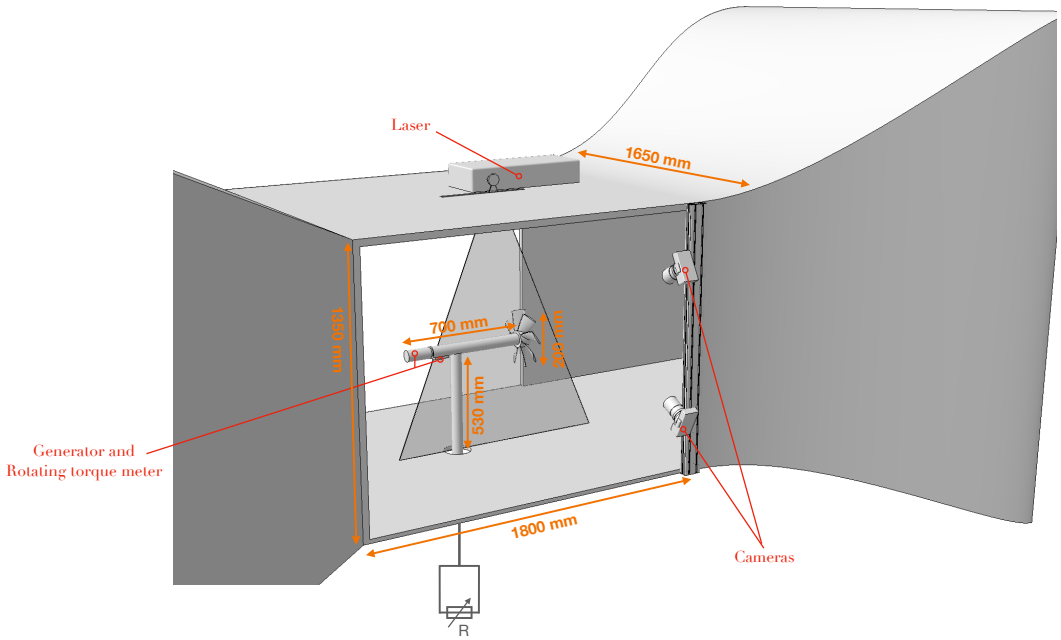

Figure 4: Wind tunnel schematic diagram with the experimental optical setup for SPIV recording and with the equipment for performance acquisitions (C_p vs. λ and C_τ vs. λ)

near wake of each rotor by stereoscopic particle image velocimetry (SPIV). The SPIV measurements are carried out for three tip-speed ratios $\lambda = 0.5$, $\lambda = 1$ and $\lambda = 1.4$ for all six rotors. The test bench to obtain the performance of the rotors is described in § 3.1 and the experimental setup for SPIV is presented in § 3.2.

3.1. Test bench for aerodynamic performance

The experimental studies were conducted in the wind tunnel of the *LIFSE* facilities. The closed circuit wind tunnel has a 3 m diameter axial fan driven by a frequency controlled 120 kW asynchronous motor. Behind the nozzle, the flow is slowed down and straightened in the settling chamber equipped with honeycomb layer and wire mesh in order to increase the flow uniformity and to decrease turbulence level before being led in the nozzle and test chamber. The nozzle has a contraction ratio of 12.5 which ensure a velocity profile with a turbulence ratio lower than 0.25% [34]. The semi-open test section has a 1.35×1.65 m^2 cross-section and is 1.8 m long. The wind speed can reach 40 m.s^{-1}. Then, the flow is slightly decelerates in a 10 m length diffuser with a 3° half angle. A schematic diagram of the experimental setup for the SPIV recordings and for the performance acquisitions is presented in Fig.4.

Inside the wind tunnel, a pitot transducer Furness Control FC20 was used to measure the dynamic pressure. The air temperature and atmospheric pressure were monitored during acquisitions in order to adjust the daily air density and therefore the upstream wind velocity. The sets were performed at fixed freestream wind speed $V_\infty = 15$ m.s^{-1} [in order to keep the Reynolds number constant during the acquisitions]. Tip-speed ratio variations were completed by changing the angular velocity of the rotor between each sample. The rotor was mounted on a shaft coupled with a MAXON DC motor. The motor was used as a brake system inside the nacelle of the turbine model. The control of the resisting torque was made by changing the electrical load on the generator with a resistor.

The torque τ was measured using a rotating torquemeter HBM-TW20 settled between the turbine and the motor. The torque transducer has a range of 2 N.m and an accuracy of 0.002 N.m. Prior to undertaking the measurements, the static torque was systematically collected and then removed during data processing. The rotor angular velocity ω was also measured by the rotating torquemeter.

The angular velocity and the wind velocity were quasi-steady during a sample. For each sample, the arithmetic average of torque, angular velocity, dynamic pressure and temperature were collected from 50 s acquisition with a sample frequency of 1000 Hz. A change in the frequency or in the acquisition time has no significant effect on the results. Between each sample, the electrical load was changed to move to another steady operating tip-speed ratio. This procedure was repeated to get the full $C_p - \lambda$ and $C_\tau - \lambda$ curves for each rotor.

The experimental procedure were carried out three times on different days for each runner to check the repeatability. For each test, the full C_p and C_τ curves were obtained. The data from these acquisitions were gathered and plotted on a single graph showing the variation in C_p and C_τ

with the tip-speed ratio for all six rotors. The results are presented in § 4.1.

3.2. Test bench for wake analysis

The phase averaging stereoscopic particle image velocimetry technique was employed to investigate the flow velocity distributions in the wake of the runners. An exhaustive description of the physical and technical backgrounds of this measurement technique is depicted in § 2 of Ref.[35]. This technique was carried out at $V_\infty = 15$ m.s^{-1} for three tip-speed ratio $\lambda = 0.5$, $\lambda = 1$ and $\lambda = 1.4$ for all six rotors. The SPIV system used in this study was handled by the software DynamicStudio 3.41 edited by Dantec. Image processing was performed with the version 4.15.

Prior to data collection, the calibration procedure was undertaken to combine 2D vector fields into a 3D vector field. A calibration target with a grid of markers were placed in the rotor axis plane and displaced from $z = 0$ to $z = \pm 3$ mm with a 0.5 mm step. For each translation, a pair of images was recorded. In addition, 13 calibration pairs images were taken. The pinhole camera model was used for both cameras to describe the mapping of points from object space to the image plane. The average reprojection error was under 0.4 pixels that is below the maximum value recommended by the software editor [36].

During an acquisition, the flow was seeded with micro-droplets of oil produced by the oil mist generator 10F03 Dantec. These droplets are supposed to strictly follow the flow without disturbing it. The particles were illuminated twice within a 90 μs time interval with a Nd-Yag laser (Litron Nano-L 200-15). The laser sheet was parallel to the rotor axis and the cameras target the upper part of the rotor. The light scattered by the particles was recorded by two cameras, supplied with Micro-Nikkor AF 60 mm f/2.8D lenses. The CCD cameras have a resolution of 2048 × 2048 pixels and were equipped with a Scheimpflug system to improve image sharpness. Both wind speed and angular velocity were steady during image acquisitions. 500 double frame images were recorded with a frequency of 2 Hz. A variation in the frequency or in the number of acquired images from 200 to 500 led to a modification of the averaged velocity fields below 5% after data processing.

The velocities from the particle images were computed in DynamicStudio software using an adaptive PIV algorithm. The recorded double frame pictures were divided in small areas, called interrogation windows, of 32×32 pixels where the velocity fields were reconstructed by measuring the local displacement of the particles between the two illuminations by cross-correlation algorithm. The mathematical background of this procedure is detailed in § 4 of Ref.[35]. The specificity of the method is that the algorithm adjusts the size and shape of the interrogation windows in order to adapt the local seeding densities and the flow gradients. Then, the 3D velocity fields were reconstructed with the rotation and translation matrix obtained from the calibration procedure. The phase averaged velocity fields in the near wake of the runners were then collected by computing the arithmetic average on each velocity components from the 500 vector velocity maps.

The same procedure was repeated for all six rotors and tip-speed ratio. Moreover, two sets of acquisitions were performed on different days to ensure the repeatability of the measurement technique. The discrepancy in the phase averaged velocity fields between the two acquisitions were below 5% in the area of interest. For the data analysis, the reference frame origin is set at the intersection of the rotation axis and the blade leading edge. The results and analysis of the averaged velocity fields are presented in § 4.2.

4. Results and discussion

The experimental results and analysis of the performance of all rotors are presented in § 4.1. It includes a discussion on the effect of the blade solidity on the power coefficient C_p and torque coefficient C_τ for various tip-speed ratio. Then, the near wake of the runners are deeply analysed in § 4.2. It contains a comparison of the induction factors and flow deflection for various blade solidity and tip-speed ratio.

4.1. Performance analysis

4.1.1. Power coefficient results C_p

Fig.5a shows the variation of the power coefficient C_p with the tip-speed ratio λ for all six micro-scale wind turbines. The tip-speed ratio range of operation is nearly the same for all rotors ($0 \leq \lambda \leq 1.7$), except for the lowest blade solidity turbine $\sigma = 0.5$ (•) which achieves a lower maximum tip-speed ratio ($\lambda_{max} = 1.6$). The maximum operating tip-speed ratio at the studied freestream wind velocity is limited by the friction of the shaft components. There is little discrepancy in the power coefficient magnitude and variation with the tip-speed ratio for high-solidity rotors ($\sigma \geq 1$) in the range $0 \leq \lambda \leq 0.75$ but low solidity rotors ($\sigma \leq 0.75$) present lower power coefficient. The maximum power coefficients $C_{p,max}$ are obtained for $\lambda_{opt} = 1$ for all wind turbines except for $\sigma = 0.5$ ($\lambda_{opt} = 1.15$). Contrary to the findings in Refs. [15, 16, 27, 31] we did not find a significant decrease in the optimum tip-speed ratio with an increase in blade solidity. However, these previous studies have focused on larger wind turbines operating at higher tip-speed ratio, therefore the range and magnitude of blade solidity is significantly lower and the actual results can hardly be replicated to fast wind turbines.

At high tip-speed ratio $\lambda \geq 1$, the rotor with the configuration $\sigma = 1.25$ (+) presents higher power coefficient than all other runners. Moreover, the $C_p - \lambda$ curves of high-solidity rotors appear flatter than those of low solidity. This specificity is valuable because a deviation from

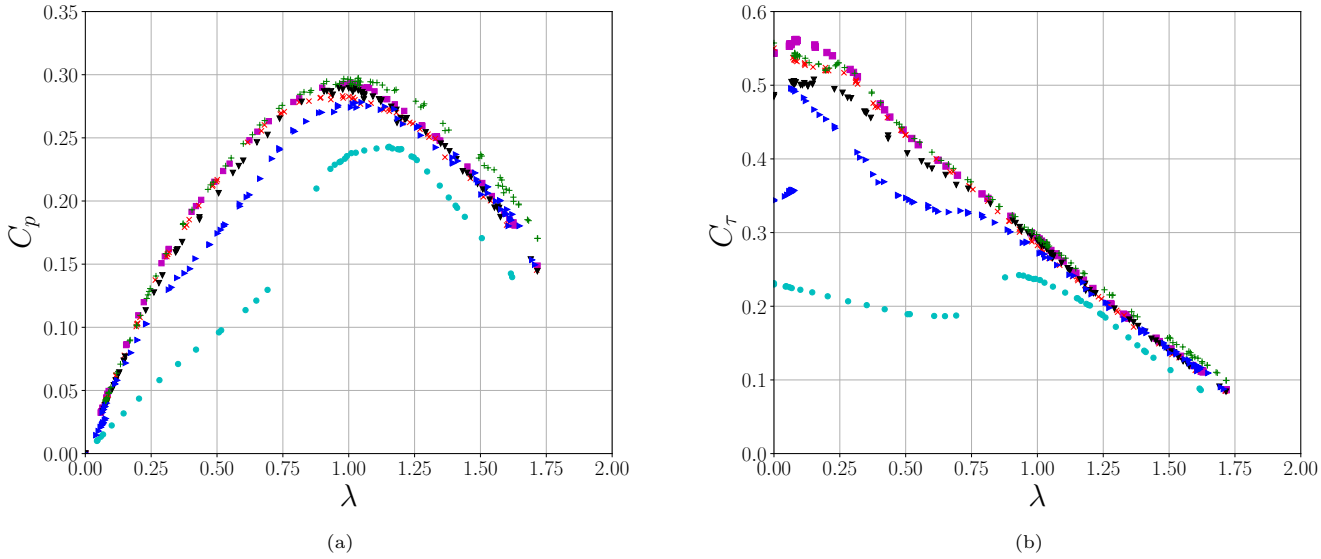

(a) (b)

Figure 5: Power coefficient C_p (a) and torque coefficient C_τ (b) as a function of the tip-speed ratio λ for $\sigma = 1.5$ (×), $\sigma = 1.25$ (+), $\sigma = 1$ (■), $\sigma = 0.75$ (▶), $\sigma = 0.5$ (●) and $\sigma = 1.65 - 0.7$ (▼). The curves are obtained from the gathering of three experimental data sets. The experiments were performed at fixed free stream wind velocity $V_\infty = 15$ m.s^{-1} on different days.

the optimum operating tip-speed ratio will not affect dramatically the performance of high-solidity runners. On the contrary, narrower $C_p - \lambda$ curves indicate a greater reduction of the performance beside the optimum tip-speed ratio. Contrary to the findings of Eltayesh et al. in Ref.[16], the current results suggest that a decrease in the blade solidity at fixed number of blades leads to produce narrower power curve. Nevertheless, the authors changed the number of blades and not the chord length in their study. Consequently, these parameters don't affect equally $C_p - \lambda$ curves and a special care must be taken to study their effect on performance independently to get relevant findings.

Fig.6a shows that an increase in the blade solidity lead to higher maximum power coefficient $C_{p,max}$. The mean blade solidity $\bar{\sigma} = 1.175$ is used for the x-axis value of the rotor with variable solidity. The maximum power coefficient $C_{p,max} = 0.29$ is achieved by the rotor with $\sigma = 1.25$. The trend of $C_{p,max}$ vs. σ plot emphasises that an excessive blade solidity induces a decrease in $C_{p,max}$, probably due to higher blockage effect. The experimental results bring consistency to the findings reported by Duquette et al. in their experimental and numerical investigation [15] who suggest the existence of an optimum blade solidity for highly bladed wind turbines.

In addition, the maximum power coefficient differs by approximately 23% from the theoretical one. This discrepancy is broadly analysed and discussed with the results from the SPIV measurements in § 4.2.

4.1.2. Torque coefficient results C_τ

The variability of the torque coefficient C_τ versus tip-speed ratio λ for all six runners is depicted in Fig.5b. Two major features are discernable.

Firstly, higher torque coefficients are obtained with high-solidity rotors but the discrepancy between rotors is mostly noticeable at low tip-speed ratio $\lambda \leq 1$. A similar pattern of results was obtained in Refs.[16, 30]. For $\lambda \geq 1$, there is very few differences in C_τ and C_p between the runners except for the one with $\sigma = 0.5$. The difference in C_τ between the runners with the configuration $\sigma = 1.25$ and $\sigma = 0.5$ decreases from $\Delta C_\tau = 0.329$ at $\lambda = 0$ to $\Delta C_\tau = 0.04$ at $\lambda = 1.4$. It emphasizes that the aerodynamic torque is less affected by an increase in blade solidity at high tip-speed ratio.

This finding can be explained by adopting a blade element approach. For a constant wind speed, a decrease in the tip-speed ratio induces an increase in the angle of attack α (please see the velocity triangle in Fig.1) and therefore an increase in the airfoil lift and drag coefficients until the stall angle. The net aerodynamic force acting of an airfoil is equal to the local lift and drag forces integrated over the airfoil exposed area. Thus, an increase in blade solidity at fixed number of blades *i.e.* in the blade chord length increases the aerodynamic forces on the airfoil and therefore the aerodynamic torque on the runner. It explains the highest amount of torque coefficient of high-solidity rotors at low tip-speed ratio. At high tip-speed ratio, the angle of attack are lower and thus the aerodynamic forces and torque decreases, which explains the slightest effect of the solidity on the torque coefficient. As will be discussed later, an increase in the the blade solidity could also postpones the stall of the lift coefficient to high angle of attack.

The aerodynamic properties of an airfoil strongly depend on the Reynolds number Re. An increase in Re

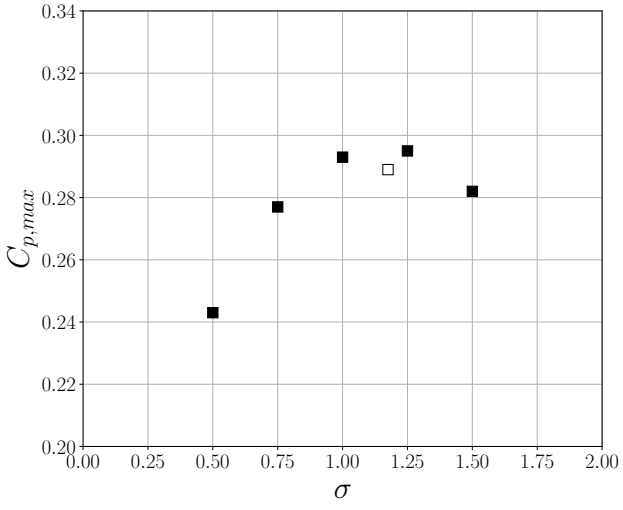

(a)

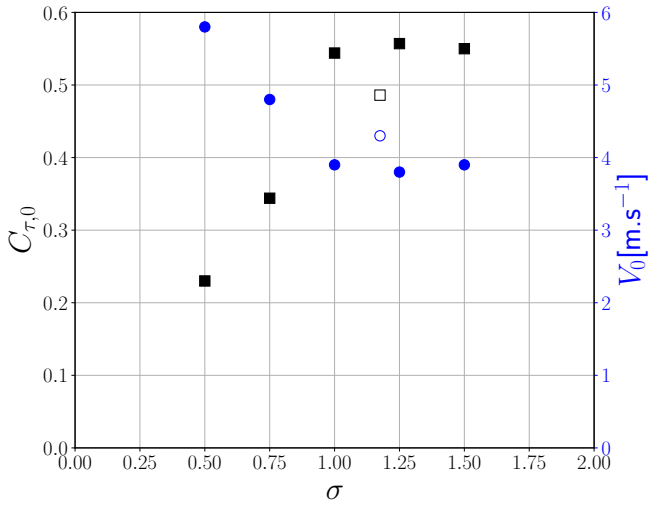

(b)

Figure 6: Effect of the blade solidity on the maximum power coefficient $C_{p,max}$ (a) and on the cut-in wind speed V_0 (•) and torque coefficient at $\lambda = 0$: $C_{\tau,0}$ (■) (b). The mean blade solidity $\sigma = 1.175$ is retained for the wind turbine with a variable solidity (hollow points)

leads to higher lift coefficient and lower drag coefficient [37–39]. Due to larger chord length, high-solidity runners operate in higher Reynolds number than low-solidity runners. For instance, the latter is three times increased from $\sigma = 0.5$ to $\sigma = 1.5$ (second part of Tab.1). It may partially contributes to higher aerodynamic forces applied on high-solidity rotors and therefore to higher torque coefficient.

Secondly, the variation of C_τ with the tip-speed ratio differs from high-solidity to low-solidity rotors. Rotors with the highest blade solidity $\sigma = 1.5$ (×) and $\sigma = 1.25$ (+) achieve their maximum torque coefficients for $\lambda = 0$. Additionally, highest solidity rotors present a nearly linear evolution of their torque coefficient with the tip-speed ratio for their full range of operation *i.e.* a linear response of their angular velocity to a resisting torque control strategy. The wide range of torque coefficient, from $C_\tau \approx 0.55$ at $\lambda = 0$ to $C_\tau \approx 0.1$ at $\lambda = 1.7$ emphasises that high-solidity rotors present a sensitive response of their angular velocity with a resisting torque control strategy. This specificity is particularly interesting for power management of electric devices because the power output of these turbines could be regulated with accuracy by varying their angular velocity [40].

On the contrary, the lowest solidity runners $\sigma = 0.5$ (•) and $\sigma = 0.75$ (▶) reach their maximum torque coefficient at $\lambda \neq 0$ (Fig.5b). The variation of C_τ with the tip-speed ratio is no longer linear but the results show a significant drop in the torque coefficient at $\lambda = 0.1$ for the runner with $\sigma = 0.75$ and at $\lambda = 0.9$ for the runner with $\sigma = 0.5$. The latter does not have steady operating point in a wide range of tip-speed ratio $0.7 \leq \lambda \leq 0.9$. A similar pattern of results was found in preliminary experiments carried out with a low solidity 3-bladed fast wind turbine [11]. In both cases, no steady experimental C_p and C_τ points are displayed for a wide range of tip-speed ratio.

An explanation, based on airfoil theory and polar plots, is postulated to analyse this finding. The blades of low-solidity rotors don't overlap and operate almost independently from each others. Therefore, the rotor acts like a sum of isolated airfoil and its aerodynamic properties are rather close to those displayed in airfoil polar plots. For instance, the variations of C_τ with the tip-speed ratio are similar to the lift coefficient variations with the angle of attack of isolated airfoils. When the tip-speed ratio decreases from $\lambda = 1.6$ to $\lambda = 0.9$, the angle of attack increases as well as the lift force on the blades and the torque coefficient.

However, too high angle of attack can lead to the separation of the flow on the upper surface of the airfoil due to[o] a high adverse pressure gradient. Both drag and lift coefficients become unsteady that induces a dramatic decreases of the aerodynamic properties of the airfoil and specifically a stall of the lift force. The boundary layer separation starts at a specific angle, called the stall angle. It depends, in particular, on the shape of the airfoil and on the Reynolds number. The rotor with $\sigma = 0.5$ starts to stall for $\lambda \approx 0.9$. This is manifested by the drop of its

torque and power coefficients and by the absence of steady C_τ and C_p experimental points for $0.9 \leq \lambda \leq 0.7$. After the critical angle, the drag forces become higher and increases with the angle of attack that explains the increase in C_τ for $\lambda \leq 0.7$.

The stall of the rotor with $\sigma = 0.75$ is also noted and starts at lower tip-speed ratio $\lambda \approx 0.75$. Indeed, its torque coefficient is constant in $0.6 \leq \lambda \leq 0.75$ instead of increasing with the angle of attack. A similar pattern is observed with higher solidity rotors but their drops in C_τ are significantly lower and occur at very low tip-speed ratio. For instance, a very limited drop in C_τ appears at $\lambda = 0.25$ for the two highest solidity rotors $\sigma = 1.5$ and $\sigma = 1.25$. Our results suggest that an increase in blade solidity postpones the stall to higher angle of attack and mitigates the aerodynamic performance drop. The effect of the stall on the performance of high-solidity rotors is offset by the high amount of drag and lift forces on the blades at low tip-speed ratio *i.e.* at high angle of attack.

The stall and the aerodynamic properties of an airfoil are affected by the Reynolds number. At high Reynolds numbers ($Re > 10^6$), the transition of the boundary layer from laminar to turbulent takes place before laminar separation but at low Reynolds it occurs during the transition [41]. Micro-scale wind turbines operate at low Reynolds number and are subject to significant unsteady phenomena, such as laminar separation bubbles (LSB). They can extend across 15% of the airfoil surface and increase dramatically the drag force [37]. Previous studies have almost exclusively focused on the effect of the Reynolds number on isolated airfoil. However, it might not similarly affect the performance of a blade cascade. This could well be the subject of future studies.

The almost absence of drop in C_τ for high-solidity rotors demonstrates that the adverse effect of LSB on the aerodynamic properties remains limited. It confirms that airfoils in high-solidity blade cascade are no longer isolated but interact with each other. The results suggest that a decrease in blade spacing reduces the formation of large recirculation bubble. In other words, the containment of the flow into a high-solidity blade cascade limits the size of LSB and the stall effects.

4.1.3. Cut-in wind speed results V_0

The starting behaviour of micro-scale wind turbines is a complex subject because it is an unsteady state that occurs at very low Reynolds number and high angles of attack [42, 43]. Even though, the previous findings on the runner operating at low tip-speed ratio are still consistent at $\lambda = 0$ (§ 4.1), there is also an additional mechanical inertia effect that can affect the runner starting behaviour. The effect of solidity on the cut-in wind speed V_0 and on the starting torque coefficient $C_{\tau,0} = C_\tau(\lambda = 0)$ is illustrated in Fig.6b. The cut-in wind speed decreases with the blade solidity from $V_0 = 5.8$ m.s^{-1} at $\sigma = 0.5$ to $V_0 = 3.8$ m.s^{-1} at $\sigma = 1.25$. These findings are consistent with the increase of the starting torque coefficient from $C_{\tau,0} = 0.230$ at $\sigma = 0.5$ to $C_{\tau,0} = 0.557$ at $\sigma = 1.25$. The [ratio $V_0^2/C_{\tau 0}$] product $V_0^2 \times C_{\tau 0}$ which corresponds to the torque required to start the rotation *i.e.* to overtake friction torque in the bearings is roughly constant for all wind turbines, which supports the consistency of the reported values of cut-in wind speed V_0.

The result suggest that the runner with a blade solidity $\sigma = 1.25$ has the best starting behaviour. However, very few discrepancies in C_τ and V_0 are noticeable from $\sigma = 1$ to $\sigma = 1.5$. A further increase in solidity could badly affect the cut-in wind speed and starting torque coefficient. An increase in solidity at fixed number of blades induces larger chord length and therefore a growth of the runner mechanical inertia. The additional mechanical inertia may not be balanced by the supplementary torque. It can lead to an increase of the cut-in wind speed.

4.2. Wake analysis

The investigation of the velocity distributions in the near wake was carried out for three tip-speed ratios $\lambda = 0.5$, $\lambda = 1$ and $\lambda = 1.4$ for all six rotors. For further details, all data collected from the SPIV measurements are available in the supplementary materials (velocity fields and profiles for all rotors and tip-speed ratios). Typical axial C_{z2} and tangential $C_{\theta 2}$ phase averaged velocity fields collected from the SPIV recordings are shown in Fig.7. In this example, the rotor with the blade solidity $\sigma = 1.25$ was operating at $\lambda = 1$ and $V_\infty = 15$m.s^{-1}. The phase averaged tangential velocity field shows that the rotor has a highly rotating and stable wake compared to conventional wind turbine as reported in Ref. [11]. It persists over 3 diameter and is very slightly disturbed. The near wakes are strongly persistent for all six rotors and tip-speed ratios. Therefore, the comparisons between them are conducted at the dimensionless horizontal distance $z/R_T = 2/3$ from the blade leading edge.

The axial and tangential induction factors radial distributions are calculated according to the Eqs.A.9&A.10 with the axial and tangential velocity fields. The effect of the blade solidity on the arithmetic average axial and tangential induction factors for various tip-speed ratio is highlighted in Fig.8. The arithmetic averages are computed for $0.3 \leq r/R_T \leq 0.9$ in order not to take into account the blade tip-losses induced by the finite span of the blades.

4.2.1. Axial induction factor a

What is striking in Fig.8a is the increase in the axial induction factor with the blade solidity for all tip-speed ratios. Moreover, the figure reveals that an increase in the tip-speed ratio induces a decrease in the axial induction factor *i.e.* a decrease in the axial velocity in the wake. It underlines that there is lower deceleration of the flow at high tip-speed ratio and for low-solidity turbines.

The radial variations of the axial induction $a(r/R_T)$ for all rotors and tip-speed ratio are depicted in Fig.9a. The

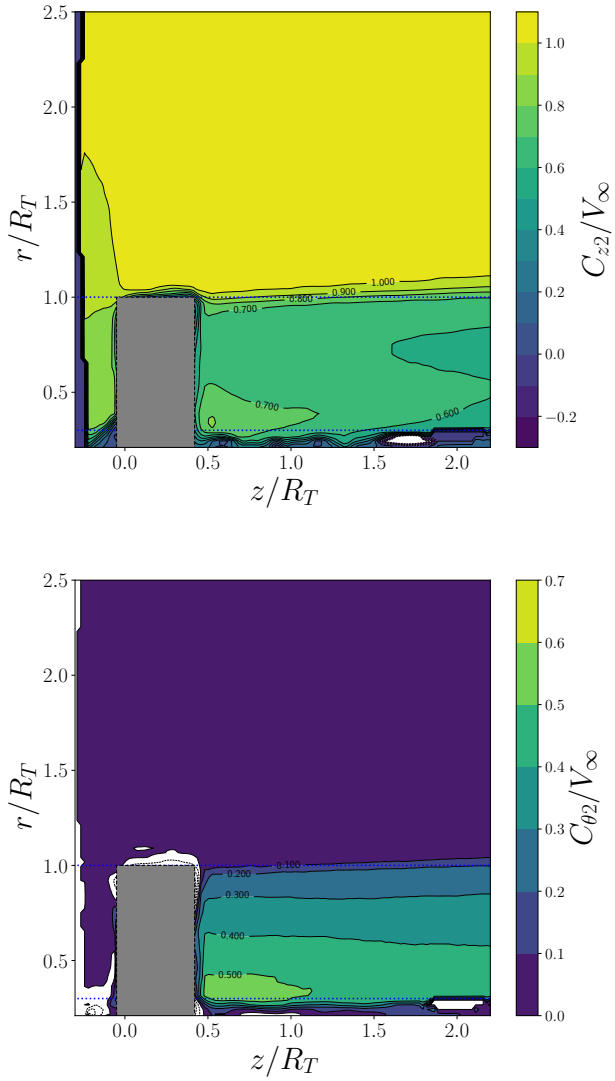

Figure 7: Dimensionless axial (up) and tangential (down) phase averaged velocity fields for the rotor with $\sigma = 1.25$ operating at $\lambda = 1$ and $V_\infty = 15\text{m.s}^{-1}$ obtained from SPIV acquisitions. 500 double frame images were recorded for average velocity computation. The reference frame origin is set at the intersection of the rotation axis and the blade leading edge

rotors were operating at $\lambda = 0.5$ in the first row, $\lambda = 1$ in the second row and $\lambda = 1.4$ in the third row. The axial induction factor profiles emphasised the general pattern of the increase in a with the blade solidity. However, the disparities in $a(r/R_T)$ between rotors varies with the tip-speed ratio. For $\lambda = 1$ and $\lambda = 1.4$, the patterns of radial variation in a are quite similar between rotors but larger discrepancies are observed at $\lambda = 0.5$. Indeed, significant fluctuations in a from root to tip are observed at low tip-speed ratio whereas it becomes increasingly constant with λ.

The upper figure in Fig.9a shows that the peak values of a are reached at the root and tip of the blade for $\lambda = 0.5$. This means, that the maximum deceleration of the flow occurs near the hub and the tip of the rotor. On the other hand, the flow deceleration reaches a peak at the middle of the span for the two others tip-speed ratio. Moreover, the figure shows that the tip leakage region increases with the tip-speed ratio. This means that the active part of the blade decreases with λ. Indeed, for $\lambda = 1.4$, the fast decreases in a near the tip starts at a lower dimensionless spanwise coordinate, especially for high-solidity rotors. It illustrates also that the tip-losses are higher at high tip-speed ratio and for high-solidity rotors. The discrepancy in tip-losses between rotors could be attributed to the larger blade thickness of high-solidity rotors that induces larger tip vortices and therefore larger losses in mechanical power. The use of a surrounding shroud for the rotor could decreases tip-losses. For instance, some authors use diffusers able to channel the flow to enhance the performance of their rotor [44, 45].

At the optimum tip-speed ratio $\lambda = 1$, the two highest solidity rotors have remarkably similar radial variation in a and an equal mean value $\overline{a}$, very close to the design induction factor (Fig.8a). Moreover, a is quasi constant in the undisturbed area of the blade, as it is set in the design method. The figures shows also that for the design tip-speed ratio, the maximum $\overline{a}$ is reached with $\sigma = 1.25$ and remains constant. Therefore, these finding suggests that the axial induction factor will probably level off or drop sharply with an additional increase in the chord length.

Finally, there is larger discrepancy in $a(r/R_T)$ between $\sigma = 1.5$ and $\sigma = 1.25$ for $\lambda = 1.4$ than for $\lambda = 1$. The results suggest the effects of the blade solidity on the distribution of axial induction factor are enhanced apart from the nominal operating point.

4.2.2. Tangential induction factor a'

Fig.9b shows the spanwise variation of the tangential induction factor $a'(r/R_T)$for the dimensionless horizontal distance $z/R_T = 2/3$ from the blade leading edge.

First, what stands out in this figure is the increase in the average tangential induction factor $\overline{a'}$ with the blade solidity for all tip-speed ratios. It's also apparent that the main differences in a' occur when the blade solidity increases from $\sigma = 0.5$ to $\sigma = 1$. An interesting finding is

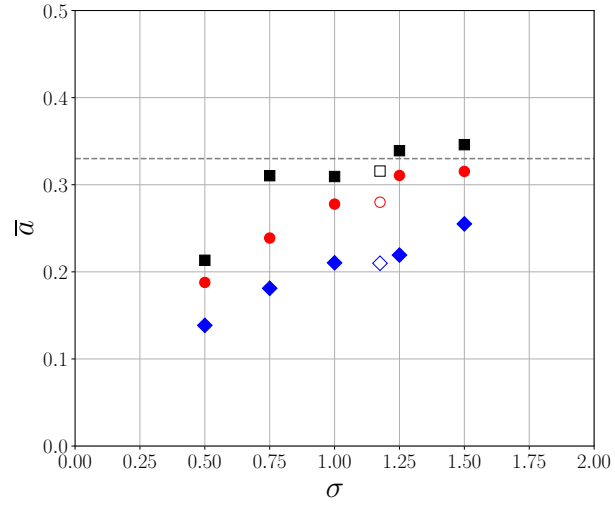

(a)

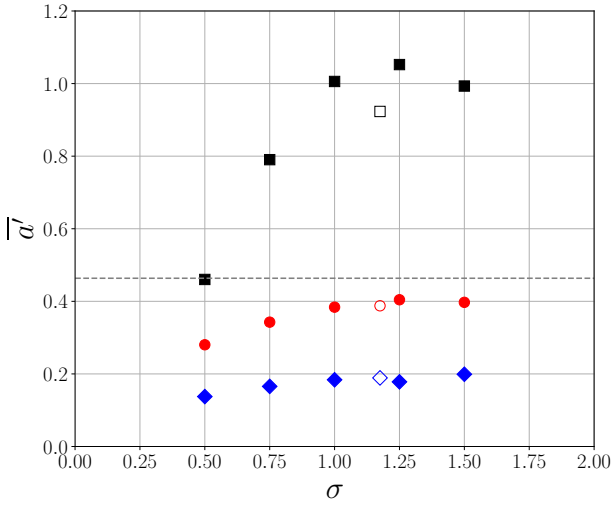

(b)

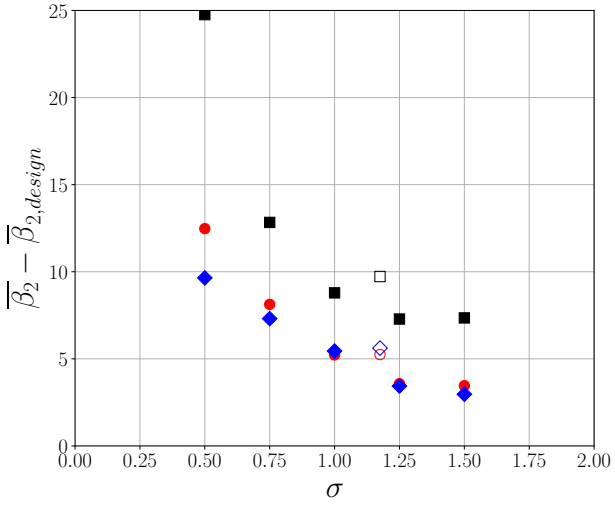

(c)

Figure 8: Effect of the blade solidity on the mean axial induction factor $\overline{a}$ (a), on the mean tangential induction factor $\overline{a'}$ (b) and on the mean deviation $\overline{\beta_2} - \overline{\beta}_{2,design}$ (c) for $\lambda = 0.5$ (■), $\lambda = 1$ (●) and $\lambda = 1.4$ (◆). The mean blade solidity $\sigma = 1.175$ is retained for the wind turbine with a variable solidity (hollow points)

that $\overline{a'}$ rises to maximum value and then remains quasi-uniform for $\lambda \geq 1$. On the contrary, Fig.8b shows that the higher $\overline{a'}$ is reached with $\sigma = 1.25$ for $\lambda = 0.5$. Moreover, it is clear from figures Figs.8b & 9b that the distributions of $a'(r/R_T)$ of the two highest solidity rotors are very similar, especially for $\lambda = 1$ and $\lambda = 0.5$. Only a small drop near the root is noticeable. The profiles are also highly similar between the highest solidity rotors at the design tip-speed ratio $\lambda = 1$.

Secondly, the average tangential induction factor decreases with the tip-speed ratio. The computation of mean tangential induction factor $\overline{a'}$ for all rotors and tip-speed ratio corroborates this finding (Fig.8b). For instance, it increases from $\overline{a'} = 0.19$ at $\lambda = 1.4$ to $\overline{a'} = 1.05$ at $\lambda = 0.5$ for the runner with $\sigma = 1.25$. Thus, higher amount of tangential velocity in the wake are produced at low tip-speed ratio. Moreover, one can notice that there is higher amount of tangential velocity at the root of the rotor than at the tip (Fig.9b). These findings are corroborated with the tangential speed profiles presented in the supplementary materials. The speed profiles show also that the tangential velocity in the wake is quasi-uniform along the span when the rotors operate at $\lambda = 0.5$. The decrease in a' depicted in Fig.9b is explained, in part, by the increase in the radial coordinate and the definition of a' (see Eq. A.9).

Finally, the main discrepancies in a' between rotors occur at the lowest tip-speed ratio $\lambda = 0.5$. For this tip-speed ratio, the angle of attack is high, therefore the near wake is more disturbed and the effect of the solidity is enhanced.

4.2.3. Flow deflection and torque

The relative angle β_2 between the relative velocity W_2 and the rotor plane is computed according to Eq. 4 with the induction factors collected from the SPIV measurements. The deflection of the fluid in the blade cascade arrangement depends on the ratio of the axial induction factor to the tangential induction factor along the span.

Fig.8c shows the variation of $\overline{\beta_2} - \overline{\beta}_{2,design}$ with the blade solidity for all studied tip-speed ratio where $\overline{\beta_2}$ is the measured arithmetic average relative angle of the flow for $z/R_T = 2/3$ and $\overline{\beta}_{2,design}$ the design arithmetic average geometric angle (Fig.2). This figure shows that an increase in tip-speed ratio or blade solidity decreases the difference between $\overline{\beta_2}$ and $\overline{\beta}_{2,design}$. Few discrepancies are noticed between the sets at $\lambda = 1$ and $\lambda = 1.4$ for high-solidity rotors ($\sigma \geq 1$). On the contrary, the blade deflection increases with λ for low-solidity rotors ($\sigma \leq 0.75$).

Moreover, the discrepancy between the average outlet geometric angle and the average relative angle of the flow is very low for $\sigma = 1.25$ and $\sigma = 1.5$ at $\lambda = 1$ and $\lambda = 1.4$ ($\overline{\beta_2} - \overline{\beta}_{2,design} \approx 3°$). These finding suggest that the flow follow more strictly the geometric deflection imposed by the blade cascade at high tip-speed ratio and when the blade solidity is high enough. Moreover, an increase in the blade solidity from $\sigma = 1.25$ to $\sigma = 1.5$ does not

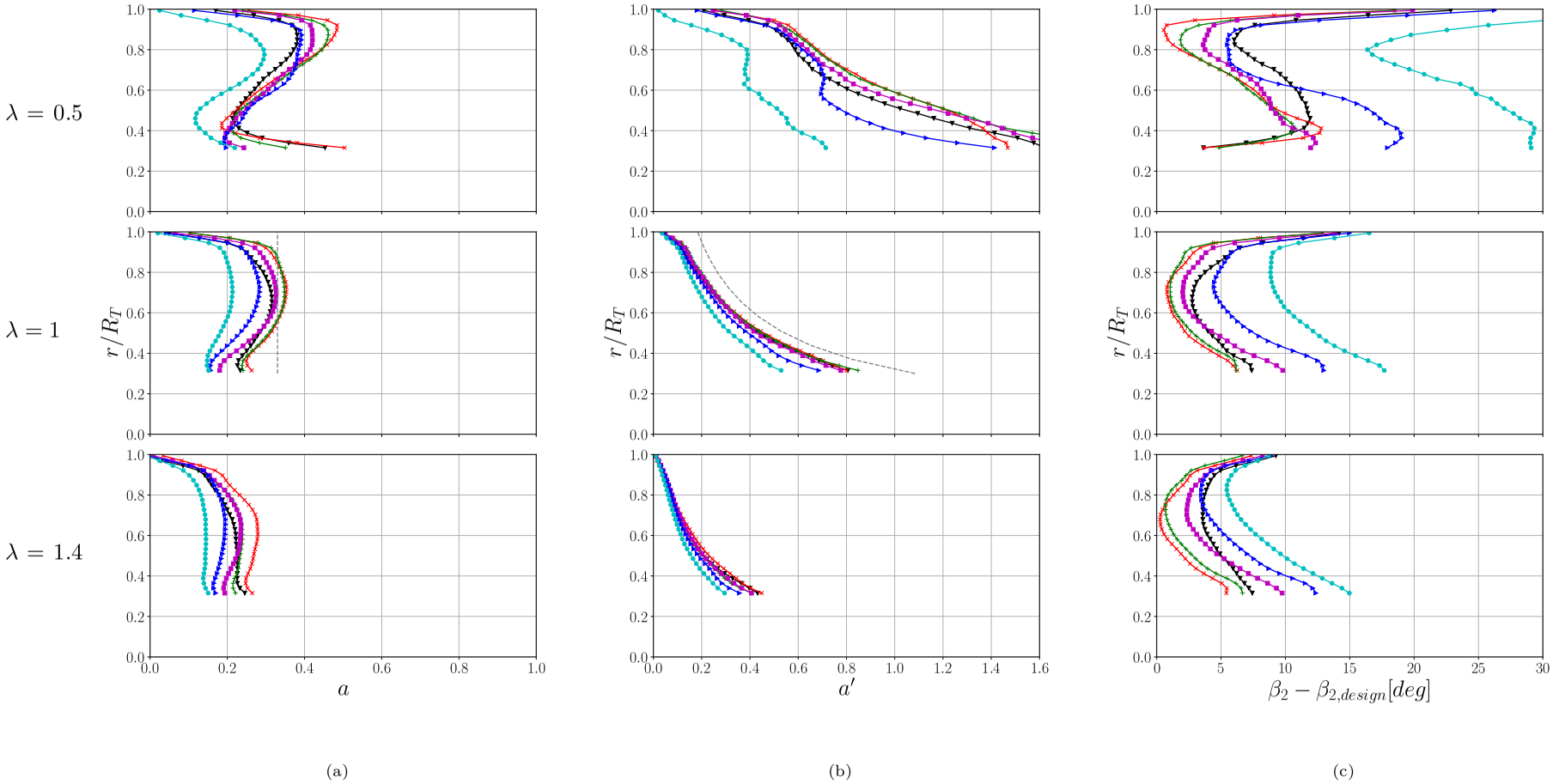

Figure 9: Axial induction factor a (a), tangential induction factor a' (b) and the difference between the experimental and design outlet relative flow angle $\beta_2 - \beta_{2,design}$ (c) vs. normalised radial coordinate for six runners with various blade solidity: $\sigma = 1.5$ (×), $\sigma = 1.25$ (+), $\sigma = 1$ (■), $\sigma = 0.75$ (▶), $\sigma = 0.5$ (●) and $\sigma = 1.65 - 0.7$ (▼). The induction factors and angles are computed from the analysis of SPIV acquisitions at the horizontal distance $z = 2R_T/3$ from the blade leading edge. The sets were performed at $V_\infty = 15\text{m.s}^{-1}$ for three tip-speed ratio $\lambda = 0.5$ (1^{st} row), $\lambda = 1$ (2^{nd} row) and $\lambda = 1.4$ (3^{rd} row). The dashed lines (−−) correspond to the design induction factor distributions

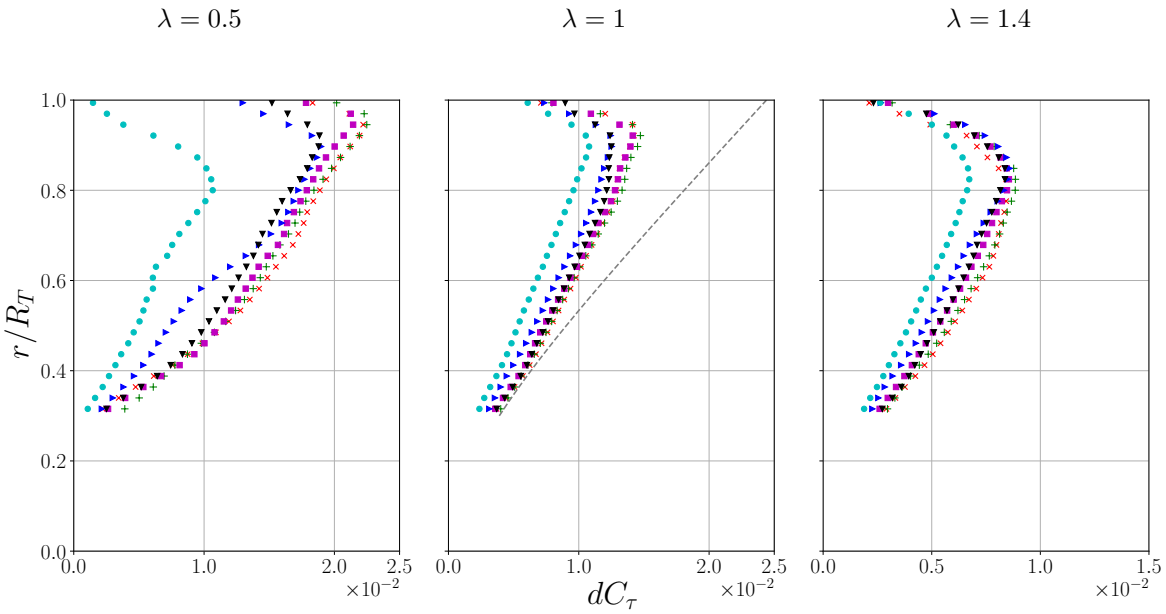

Figure 10: Infinitesimal torque coefficient vs. dimensionless radial coordinate for six runners with various blade solidity: $\sigma = 1.5$ (×), $\sigma = 1.25$ (+), $\sigma = 1$ (■), $\sigma = 0.75$ (▶), $\sigma = 0.5$ (●) and $\sigma = 1.65 - 0.7$ (▼). The parameters are computed from the SPIV measurements. Special care must be paid to the varying range of x-values between the three sets of acquisitions. The measurements were performed at $V_\infty = 15\text{m.s}^{-1}$ and $\lambda = 0.5$ (left), $\lambda = 1$ (middle) and $\lambda = 1.4$ (right). The dashed lines (−−) depict the design settings

improve the containment of the fluid into the blade cascade significantly while an increase from $\sigma = 0.5$ to $\sigma = 1.25$ does.

The profiles $\beta_2 - \beta_{2,design}$ vs. r/R_T in Fig.9c show the spanwise variations of the relative angle of the flow for $z/R_T = 2/3$. An increase in σ or λ also reduces the discrepancy between the distribution of β_2 set for the design of the blades and the relative angle of the flow in the near wake of the wind turbine. The flow more strictly follows the deflection of the blade cascade at $r/R_T \approx 0.7$.

The flow outlet relative angle β_2 is function of both axial and tangential induction factor (Eq.4). They don't contribute equally to the difference between the imposed and observed deflection when the rotors operate at their design tip-speed ratio $\lambda = 1$. When focusing on high-solidity turbines operating at $\lambda = 1$ (Fig.9), the axial induction factor distribution $a(r/R_T)$ is closed to the design settings from $r/R_T = 0.5$ to $r/R_T = 0.8$ but the amount of tangential induction factor is lower than the design settings. The expected blade deflection is almost reached in the middle of the span. At the root of the blade, high discrepancy between β_2 and $\beta_{2,design}$ is explained by both lower axial and tangential induction factors. This can be explained by the proximity of the nacelle and nose of the turbine. Moreover the significant difference at the tip is induced by the finite span of the blade and therefore the following flow conditions in the rotor plane: $a(1) = 0$ and $a'(1) = 0$ that are not taken into account in the design method.

The comparison of the sets performed at $\lambda = 1$ and $\lambda = 1.4$ reveals another interesting finding. Very few discrepancies are observed in $\overline{\beta_2} - \overline{\beta}_{2,design}$ and $\beta_2(r/R_T)$ between the two sets. However, as mentioned in the previous paragraphs, an increase in λ increases a and decreases a' for all runners. Therefore, the results suggest that the increase in a is balanced by the decrease in a' in order to keep the relative angle of the flow approximately constant. Moreover, for $\lambda = 1.4$, the flow behind the rotors with $\sigma = 1.5$ and $\sigma = 1.25$ is deflected equally but the induction factors are different. The wake behind the highest solidity runner has a lower axial velocity but in return a higher tangential velocity than the rotor with $\sigma = 1.25$.

The patterns of variation in β_2 differ[s] completely at $\lambda = 0.5$ from the other[s] tip-speed ratios. The maximum deflection of the flow is achieved at higher radial distance $r/R_T \approx 0.9$ and the discrepancy in β_2 from hub to tip are more significant. Moreover, near the hub, the relative angle of the flow is far from the outlet geometric angle of the blade cascade especially for low-solidity rotors.

Moreover, it is possible to compute the torque and power coefficients from the SPIV recordings by integrating the Eqs. A.8 & A.7. Fig.10 shows the variation of the infinitesimal torque coefficient dC_τ as a function of the dimensionless radial distance r/R_T. While the rotating torquemeter only provides global quantities of torque and power, the SPIV recordings allow to visualise the loading along the blade span and to understand the mechanism of torque production. The torque coefficient distribution set for the design of the blade can also be computed with the design induction factors. Its variation with the dimensionless spanwise coordinate is depicted in Fig.10 (middle figure).

For the design tip-speed ratio $\lambda = 1$, the relative deviation in global C_p and C_τ between SPIV and torquemeter

measurements are ranging from 0.3% to 2.8% for C_p and from 0.3% to 3.3% for C_τ. The maximum deviation is found for the rotor with $\sigma = 0.5$. A possible explanation is that this rotor produces less torque than the others and therefore the friction between the mechanical parts contain in the nacelle can affect more the experimental measurements. The relative difference between the total torque and power coefficients computed from SPIV and the one measured with the torquemeter is small enough to allow discussing the variation of blade loading dC_τ along the span derived from SPIV recordings.

The results presented in Fig.10 corroborates the finding presented in § 4.1. Overall, an increase in the blade solidity increases the torque coefficient for all tip-speed ratios, especially from $\sigma = 0.5$ to $\sigma = 1$. Even though the main difference in dC_τ between high-solidity occurs at $\lambda = 0.5$, a trend of increasing dC_τ with σ is also noticeable at $\lambda = 1$ and $\lambda = 1.4$. The figures shows also that for all tip-speed ratios and blade solidit[y]ies, the torque is mainly produced in the upper part of the blade. Moreover, the decrease in dC_τ starts at lower spanwise coordinate for all rotors at $\lambda = 1.4$ than at $\lambda = 1$ and $\lambda = 0.5$. It suggests that the length of the blade producing mechanical work decrease with the tip-speed ratio and therefore that higher tip-loss effect occurs at high tip-speed ratio.

The sets at $\lambda = 1$ (middle figure) show a large difference between the experimental torque distribution and the design setting especially near the tip of the blade. It highlights the limitations of the hypothesis assumed in the general momentum theory and Glauert's optimum flow model: a rotor with an infinite number of blades, an inviscid and steady flow, the independency of each annular ring and the absence of wake expansion.

Moreover, no tip-loss factor were added in the design method to consider the physical conditions $a = 0$ and $a' = 0$ at the tip. As mentioned in the § 4.2.1, a diffuser or a surrounding shroud could decreases tip-losses. However, near the root of the blades, very few discrepancies in dC_τ are observed.

Secondly, the variation of the infinitesimal torque along the span varies substantially at low tip-speed ratio $\lambda = 0.5$ between all rotors. Interestingly, from $r/R_T = 0.3$ to $r/R_T = 0.4$, the rotors with $\sigma = 1.25$ and $\sigma = 1$ produce larger amount of torque than the rotor with the highest blade solidity $\sigma = 1.5$. A possible explanation for this might be that there is too high flow blockage near the hub of the rotor with $\sigma = 1.5$ which prevents the flow to pass through the cascade and thus to produce torque.

This tendency decreases with the radial distance. From $r/R_T = 0.4$ to $r/R_T = 0.7$, there is a clear trend of increasing torque with the blade solidity. Finally, from $r/R_T = 0.75$ to $r/R_T = 0.9$, the highest amount of torque is generated by the rotors with $\sigma = 0.75$, $\sigma = 1$ and $\sigma = 1.65 - 07$. These variations can be explained with the induction factors. For all rotors, the magnitude of axial and tangential induction factors near the hub are significant. Thus the contribution of the tangential induction factor to the torque creation is substantially greater than the contribution of the axial induction factor according to the Eq. A.8. High-solidity rotors induces a highly rotating flow that explains the large production of torque near the hub. When the radial distance increases, the tangential induction factor a' decreases greatly and the axial induction factor remains constant or increases. Thus, in the upper part of the blade, the contribution of the axial induction factor to the torque creation is more significant than the tangential velocity. Low-solidity rotors have fewer axial induction factor and therefore produce more torque than high-solidity turbines in the upper part of the blades. Similar conclusions can be drawn from the sets at $\lambda = 1$ and $\lambda = 1.4$.

A further explanation of the discrepancy between the design and experimental relative angle as well as the expected and measured perfomance is that no empirical correlations where applied in the design method to correct the flow deflection. Loss and deflection models are mostly available in the literature for compressor blading [46] and for the design of pumps and impulse turbine cascade [47, 48].

Some corrections, such as Weinig's correction [49], are sometimes used for the design of high-solidity hydrokinetic turbines but they are mainly focused on the adjustment of the lift and drag coefficients during the BEMT procedures [50]. The effective losses and deviation from the geometric deflection are not taken into account in these models. Future investigations on this topic are needed to fully understand the implications of the solidity on the aerodynamic characteristic of an airfoil. The works performed on compressor show that the losses and blade deviation depend on many factors, such as the blade solidity, the angle of attack and the Reynolds number [46]. Thus, the formulation of losses and deviation laws from wind tunnel experiments could be of particular interest to improve the design method and to predict the performance of high-solidity wind turbines with accuracy.

5. Conclusion and perspectives

The aim of the present experimental research was to examine the effect of the blade solidity on the performance and near wake of low tip-speed ratio micro-scale wind turbines. Six 200 mm wind turbines with various solidity, from $\sigma = 0.5$ to $\sigma = 1.5$ were designed and manufactured by fused material deposition. Their design tip-speed ratio was set at $\lambda = 1$ and they have 8 blades. The blade angles were computed with the optimal tangential induction factor of Glauert and their chord length by assuming a constant solidity from root to tip. The full C_τ and C_p vs. the tip-speed ratio λ curves and cut-in wind speed V_0 were obtained in a wind tunnel.

This study shows that a blade solidity higher than $\sigma \geq 1$ was favorable for low tip-speed ratio micro-scale wind turbines. High-solidity wind turbines achieve higher power coefficient, of the order of $C_{p,max} = 0.3$, and have

lower cut-in wind speed than low-solidity wind turbines. Additionally, high-solidity runners present a nearly linear decrease in torque coefficient with the tip-speed ratio whereas C_τ vs. λ curves of low-solidity rotors are not strictly linear. This observation suggests that the aerodynamic behaviour of the blades differs from the behaviour of an isolated airfoil when they are placed in a high-solidity blade cascade arrangement. Another major finding emerging from this study is the presence of an optimum solidity, after which a further increase in blade solidity is not favorable. Even though, the value of the optimum solidity found in this study $\sigma = 1.25$ depends on the design tip-speed ratio, number of blades and blade angles, this study provide a range of solidity favorable for micro-scale wind turbines. In addition, high-solidity rotors designed according the current method appear to be efficient micro-scale wind energy harvesters that can be used in low wind speed conditions. The linear response of their angular velocity with a resisting torque control strategy is also beneficial for electrical applications.

The investigation of the near wake of all six wind turbines was carried out by SPIV for three tip-speed ratio $\lambda = 0.5$, $\lambda = 1$ and $\lambda = 1.4$ to examine the effects of the blade solidity and tip-speed ratio on the airflow deflection. The results of this investigation show that an increase in the blade solidity leads to higher axial and tangential induction factors for all tip-speed ratios. It highlights that high-solidity rotors induce both larger deceleration and flow rotation. Axial induction factor mean values and distributions are close to the design settings for high-solidity rotors. Larger discrepancies are observed in the tangential induction factor but the patterns of variation are also similar to the design settings. These findings emphasize the appropriateness of the design method for low tip-speed ratio and high-solidity runners even if further refinement are required. Higher fluctuations in the induction factors are observed between the run performed at $\lambda = 0.5$ than at $\lambda = 1$ and $\lambda = 1.4$ which suggests that the flow is more disturbed when the rotors operate at low tip-speed ratio. The SPIV measurements reveal also that the torque is mainly generated at the tip of the blades. Finally, the study shows that the contribution of the induction factors on the torque coefficient varies depending on the solidity of the runner, the radial coordinate of the blade and the tip-speed ratio.

Based on the experimental results and current limitations of this study, three perspectives of this work can be identified. First, the design method could be improved by adding loss and deflection models. Unfortunately, very few coefficients are available in the open literature to correct the deflection computed from the Euler's turbine theorem. Therefore, the characterisation of the deflection of the flow by a fixed blade cascade arrangement is an interesting topic for future work. A parametric study could be performed to evaluate the effect of the solidity of the cascade, the angle of attack and the Reynolds number on flow deflection efficiency. It would help to understand the interactions between blades when the space between them is reduced *i.e.*, the mutual blade interactions. These deflection laws could also be used in the classical design method to correct the airfoil aerodynamic coefficients and angle of attack when the solidity increases. Secondly, the study reveals that the performance of micro-scale wind turbines are highly affected by the tip-losses due to the finite span of the blades. Thus, the design of diffuser or shrouded turbines could help to decrease these losses by increasing the active part of a blade. Finally, the experimental investigations suggest an effect of the Reynolds number on the performance of micro-scale runners. A quantitative study on the effect of the Reynolds number on the performance and velocity distributions of a micro-scale runner by adding or removing blades with the same geometry could interest the scientific community.

References

[1] D. Carvalho, A. Rocha, X. Costoya, M. deCastro, and M. Gómez-Gesteira. Wind energy resource over europe under cmip6 future climate projections: What changes from cmip5 to cmip6. *Renewable and Sustainable Energy Reviews*, 151:111594, 2021.

[2] M. Rapin and J-M. Noël. *L'énergie éolienne. Du petit éolien à l'éolien offshore*. Dunod, 2019.

[3] E. Welfonder, R. Neifer, and M. Spanner. Development and experimental identification of dynamic models for wind turbines. *Control Engineering Practice*, 5(1):63–73, 1997.

[4] L A Viterna and D C Janetzke. Theoretical and experimental power from large horizontal-axis wind turbines. *US Department of energy*, 1982.

[5] Hiroyuki Akinaga. Recent advances and future prospects in energy harvesting technologies. *Japanese Journal of Applied Physics*, 59(11):110201, oct 2020.

[6] M. Perez, S. Boisseau, P. Gasnier, J. Willemin, M. Geisler, and J. L. Reboud. A cm scale electret-based electrostatic wind turbine for low-speed energy harvesting applications. *Smart Materials and Structures*, 25(4):045015, 2016.

[7] C.L. Zhang, Z.H. Lai, M.Q. Li, and D. Yurchenko. Wind energy harvesting from a conventional turbine structure with an embedded vibro-impact dielectric elastomer generator. *Journal of Sound and Vibration*, 487:115616, 2020.

[8] Michael A. Weimer, Thurein S. Paing, and Regan A. Zane. Remote area wind energy harvesting for low-power autonomous sensors. In *2006 37th IEEE Power Electronics Specialists Conference*, pages 1–5, 2006.

[9] Davide Brunelli. A high-efficiency wind energy harvester for autonomous embedded systems. *Sensors (Basel, Switzerland)*, 16, 2016.

[10] Davide Carli, Davide Brunelli, Davide Bertozzi, and Luca Benini. A high-efficiency wind-flow energy harvester using micro turbine. In *SPEEDAM 2010*, pages 778–783, 2010.

[11] M. Bourhis, M. Pereira, F. Ravelet, and I. Dobrev. Innovative design method and experimental investigation of a small-scale and very low tip-speed ratio wind turbine. *Experimental Thermal and Fluid Science*, 130:110504, 2022.

[12] Abhishiktha Tummala, Ratna Kishore Velamati, Dipankur Kumar Sinha, V. Indraja, and V. Hari Krishna. A review on small scale wind turbines. *Renewable and Sustainable Energy Reviews*, 56:1351–1371, 2016.

[13] Ronit K. Singh, M. Rafiuddin Ahmed, Mohammad Asid Zullah, and Young-Ho Lee. Design of a low reynolds number airfoil for small horizontal axis wind turbines. *Renewable Energy*, 42:66–76, 2012. International Symposium on Low Carbon and Renewable Energy Technology 2010 (ISLCT 2010).

[14] P.D. Clausen and D.H. Wood. Research and development issues for small wind turbines. *Renewable Energy*, 16(1):922–927, 1999.
[15] Matthew M. Duquette, Jessica Swanson, and Kenneth D. Visser. Solidity and Blade Number Effects on a Fixed Pitch, 50 W Horizontal Axis Wind Turbine. *Wind Engineering*, 27(4):299–316, 2003.
[16] Abdelgalil Eltayesh, Francesco Castellani, Massimiliano Burlando, Magdy Bassily Hanna, A. S. Huzayyin, Hesham M. El-Batsh, and Matteo Becchetti. Experimental and numerical investigation of the effect of blade number on the aerodynamic performance of a small-scale horizontal axis wind turbine. *Alexandria Engineering Journal*, 60(4):3931–3944, 2021.
[17] Sheng-Huan Wang and Shih-Hsiung Chen. Blade number effect for a ducted wind turbine. *Journal of Mechanical Science and Technology*, 22:1984–1992, 2008.
[18] Mohamed Y. Zakaria, Daniel A. Pereira, and Muhammad R. Hajj. Experimental investigation and performance modeling of centimeter-scale micro-wind turbine energy harvesters. *Journal of Wind Engineering and Industrial Aerodynamics*, 147:58–65, 2015.
[19] D A Howey, A Bansal, and A S Holmes. Design and performance of a centimetre-scale shrouded wind turbine for energy harvesting. *Smart Materials and Structures*, 20(8):085021, 2011.
[20] Dennis Leung, Y. Deng, and Michael K.H. Leung. Design optimization of a cost-effective micro wind turbine. *WCE 2010 - World Congress on Engineering 2010*, 2:988–993, 2010.
[21] JN. Sørensen. *General Momentum Theory for Horizontal Axis Wind Turbines*, volume 4 of *Research Topics in Wind Energy*. Springer International Publishing, Cham, 2016.
[22] Tony Burton, David Sharpe, Nick Jenkins, and Ervin Bossanyi. *Wind Energy Handbook*. 2002.
[23] H. Glauert. *Airplane Propellers*. Springer Berlin Heidelberg, Berlin, Heidelberg, 1935.
[24] A. Betz. *Windenergie und ihre Ausnützung durch Windmühlen*. Vandenhoeck and Ruprecht, Göttingen, 1926.
[25] D. J. Sharpe. A general momentum theory applied to an energy-extracting actuator disc. *Wind Energy*, 7(3):177–188, 2004.
[26] M.A. Khan, P. Pillay, and K.D. Visser. On adapting a small pm wind generator for a multiblade, high solidity wind turbine. *IEEE Transactions on Energy Conversion*, 20(3):685–692, 2005.
[27] Zawadzki, Karol, ´Smiechowicz, Wojciech, Stepie´n, Malgorzata, Baszczy´nska, Anna, and Tarkowski, Michal. Influence of the solidity ratio on the small wind turbine aerodynamics. *E3S Web Conf.*, 242:03006, 2021.
[28] Fabio Mendonca and Joaquim Azevedo. Design and power production of small-scale wind turbines. In *2017 International Conference in Energy and Sustainability in Small Developing Economies (ES2DE)*, pages 1–6, Funchal, Portugal, 2017. IEEE.
[29] M. Rector, K. Visser, and C. Humiston. *Solidity, Blade Number, and Pitch Angle Effects on a One Kilowatt HAWT*.
[30] Antonio Brasil Junior, Rafael Mendes, Théo Wirrig, Ricardo Noguera, and Taygoara Oliveira. On the design of propeller hydrokinetic turbines: the effect of the number of blades. *Journal of the Brazilian Society of Mechanical Sciences and Engineering*, 41, 2019.
[31] Matthew Duquette and Kenneth Visser. Numerical implications of solidity and blade number on rotor performance of horizontal-axis wind turbines. *Journal of Solar Energy Engineering*, 125:425, 2003.
[32] Salih N. Akour, Mohammed Al-Heymari, Talha Ahmed, and Kamel Ali Khalil. Experimental and theoretical investigation of micro wind turbine for low wind speed regions. *Renewable Energy*, 116:215–223, 2018.
[33] K. Bassett, R. Carriveau, and D.S.-K. Ting. 3d printed wind turbines part 1: Design considerations and rapid manufacture potential. *Sustainable Energy Technologies and Assessments*, 11:186–193, 2015.
[34] Ivan Dobrev and Fawaz Massouh. Cfd and piv investigation of unsteady flow through savonius wind turbine. *Energy Procedia*, 6:711–720, 2011.
[35] M. Raffel, C. Willert, and J. Kompenhans. *Particle Image Velocimetry: A Practical Guide*. Number 3. 2018.
[36] Dantec Dynamics. *DynamicStudio. User's Guide*. Dantec Dynamics, Skovlunde, Denmark, 2013.
[37] J. C. Muti Lin and Laura L. Pauley. Low-reynolds-number separation on an airfoil. *AIAA Journal*, 34(8):1570–1577, 1996.
[38] Shubham Jain, Nekkanti Sitaram, and Sriram Krishnaswamy. Effect of reynolds number on aerodynamics of airfoil with gurney flap. *International Journal of Rotating Machinery*, 2015, 2015.
[39] Dong-Ha Kim, Jo-Won Chang, and Joon Chung. Low-reynolds-number effect on aerodynamic characteristics of a naca 0012 airfoil. *Journal of Aircraft*, 48(4):1212–1215, 2011.
[40] Manjunath N., Mallikarjunaswamy S., Komala M., Sharmila N., and Manu S. An efficient hybrid reconfigurable wind gas turbine power management system using mppt algorithm. *International Journal of Power Electronics and Drive Systems (IJPEDS)*, 12:2501, 2021.
[41] Philippe Giguère and Michael S. Selig. Low Reynolds Number Airfoils for Small Horizontal Axis Wind Turbines. *Wind Engineering*, 21(6):367–380, 1997.
[42] P.R. Ebert and D.H. Wood. Observations of the starting behaviour of a small horizontalaxis wind turbine. *Renewable Energy*, 12(3):245–257, 1997.
[43] A.K. Wright and D.H. Wood. The starting and low wind speed behaviour of a small horizontal axis wind turbine. *Journal of Wind Engineering and Industrial Aerodynamics*, 92(14):1265–1279, 2004.
[44] Paulo A.S.F. Silva, Deborah A.T.D. Rio Vaz, Vinicius Britto, Taygoara F. de Oliveira, Jerson R.P. Vaz, and Antonio C.P. Brasil Junior. A new approach for the design of diffuser-augmented hydro turbines using the blade element momentum. *Energy Conversion and Management*, 165:801–814, 2018.
[45] Mohammad Ali Rahmatian, Pooyan Hashemi Tari, Mohammad Mojaddam, and Sahand Majidi. Numerical and experimental study of the ducted diffuser effect on improving the aerodynamic performance of a micro horizontal axis wind turbine. *Energy*, 245:123267, 2022.
[46] Luis E. Ferrer-Vidal, Marc Schneider, Alessandro Allegretti, and Vassilios Pachidis. A Loss and Deflection Model for Compressor Blading at High Negative Incidence. *Journal of Turbomachinery*, 141(12), 2019.
[47] W. R. Hawthorne, C. Wang, C. S. Tan, and J. E. McCune. Theory of Blade Design for Large Deflections: Part I—Two-Dimensional Cascade. *Journal of Engineering for Gas Turbines and Power*, 106(2):346–353, 1984.
[48] Robert REY, Ricardo NOGUERA, and Farid BAKIR. Pompes rotodynamiques aérohydrodynamique des profils et aubages de pompes hélices. *Techniques de l'ingénieur Machines hydrauliques, aérodynamiques et thermiques*, base documentaire : TIP151WEB.(ref. article : bm4304), 2013.
[49] F. S. Weinig. *Section B. Theory of Two-Dimensional Flow Through Cascades*. Princeton University Press, 2017.
[50] Antonio Brasil Junior, Rafael Mendes, Julian Lacroix, Ricardo Noguera, and Taygoara Oliveira. Hydrokinetic propeller turbines. how many blades? *American Journal of Hydropower, Water and Environment Systems*, 2, 2017.
[51] N.E. Joukowsky. *Vortex theory of a rowing screw. Trudy Otdeleniya Fizicheskikh Nauk Obshchestva Lubitelei Estestvoznaniya*, volume 16(1). 1912.

Appendix A. General momentum theory

The general momentum theory, formulated initially by Glauert in Ref.[23], allows to predict the axial, radial and tangential velocity distributions in the rotor plane by applying the conservation of mass, the axial and angular mo-

mentum balances and the energy conservation on a streamtube control volume. The full developments can be found for instance in §4 of Ref. [21].

In the general momentum theory, a streamtube that encloses the turbine is discretized into annular elements of height dr, with r the radial coordinate. The infinitesimal torque $d\tau$ applied by the disc of turbine on an annular element is computed by applying the Euler's turbine theorem to an infinitesimal control volume of thickness dr:

$$d\tau = 2\pi r\rho dr C_{z2} r C_{\theta 2} \quad \text{(A.1)}$$

with $2\pi r dr$ the cross-section area of the control volume at the rotor plane, and ρ the fluid density. The axial velocity C_{z2} and azimuthal velocity $C_{\theta 2}$ behind the rotor plane can be defined as follows:

$$C_{z2} = V_\infty(1-a) \quad \text{(A.2)}$$
$$C_{\theta 2} = 2a'\omega r \quad \text{(A.3)}$$

where a and a' are respectively the axial and tangential induction factors. Therefore, the Eq. A.1 reads:

$$d\tau = 4\pi\rho r^3 V_\infty(1-a)\omega a' dr \quad \text{(A.4)}$$

The power coefficient C_p and torque coefficient C_τ emphasise the relationship between wind power and mechanical power obtained in the turbine. The torque coefficient is a dimensionless measure of the torque produced by the turbine and the power coefficient establish power conversion rate:

$$C_p = \frac{P}{P_a} = \frac{\tau\omega}{0.5\rho\pi R_T^2 V_\infty^3} \quad \text{(A.5)}$$
$$C_\tau = \frac{\tau}{0.5\rho\pi R_T^3 V_\infty^2} \quad \text{(A.6)}$$

They are computed from the integration of the Eq. A.4 from the hub radius R_H to the tip radius R_T of the rotor:

$$C_p = 8\lambda^2 \int_{R_H}^{R_T} a'(1-a)\left(r/R_T\right)^3 \frac{dr}{R_T} \quad \text{(A.7)}$$
$$C_\tau = 8\lambda \int_{R_H}^{R_T} a'(1-a)\left(r/R_T\right)^3 \frac{dr}{R_T} \quad \text{(A.8)}$$

The Eq. A.7 shows that a maximum power coefficient can be reached for a given tip-speed ratio by optimising the relationship between a and a'.

The general momentum theory is an iterative optimising procedure of a and a'. Several models exist [21–24, 51], under various assumptions, but the one proposed by Glauert in 1935, initially for the design of propeller remains the linchpin of the Blade Element Momentum Theory [23]. Most wind turbines in the open literature are designed conforming to its model. He derived a relationship between a and a' which must be fulfilled in optimum conditions *i.e.* to reach the maximum power coefficient $C_{p,max}$:

$$a' = \frac{1-3a}{4a-1} \quad \text{(A.9)}$$

and a polynomial expression for a:

$$16a^3 - 24a^2 + 3a(3-\lambda^2 x^2) - 1 + \lambda^2 x^2 = 0 \quad \text{(A.10)}$$

where $x = r/R_T$ is the dimensionless spanwise coordinate.

Then, for a given tip-speed ratio, the Eqs. A.9 & A.10 give the optimal distributions induction factors *i.e.*, the optimal radial flow velocity distributions in the rotor plane. Moreover, the Eq. A.7 enables to determiner the upper performance limit of the rotor. For instance, in ideal flow conditions, the maximum power coefficients computed with the Glauert's model are $C_{p,max}(\lambda = 1) = 0.415$ and $C_{p,max}(\lambda = 6) = 0.576$ and the torque coefficients are $C_{\tau,max}(\lambda = 1) = 0.415$ and $C_{\tau,max}(\lambda = 6) = 0.096$.